Low-Complexity Power-Balancing-Point Based Optimization for Photovoltaic Differential Power Processing

Guanying Chu, *Student Member*, *IEEE*, Huiqing Wen, *Senior Member IEEE,* Yihua Hu, *Senior Member*, *IEEE*, Lin Jiang, *Member*, *IEEE*, Yong Yang, *Member*, *IEEE*, Yiwang Wang

***Abstract*- Differential power processing (DPP) is regarded as a promising architecture in solving mismatching issues among photovoltaic (PV) submodules. Although conventional total-minimum-power-point (TMPP) based real-time optimization algorithm by using the distributed submodule-level maximum power point tracking (MPPT) and simultaneously the centralized total-minimum-power tracking (TMPT) shows effectiveness in maximizing the power yield. However, uneven power stress among DPP converters, large oscillations, high additional cost for communication among DPP converters, and complicated implementation hinder the practical application. This paper proposed a low-complexity power-balancing-point (PBP) based optimization algorithm to reduce the system cost and size, improve the system efficiency, and realize the standardized modular design for DPP converters. Furthermore, simple submodule-level voltage equalization (VE) control is implemented to eliminate expensive communication and relieve the control complexity while guarantee high MPP efficiency. The proposed algorithm can reduce the power rating of DPP converters compared with conventional TMPP-based control, which is beneficial to the improvement of system cost, reliability and lifetime. Both simulation and experimental results under various scenarios are provided to validate the advantages of the proposed algorithm.**

***Index Terms*—Differential power processing, mismatch, partial shading, power rating, photovoltaic systems, voltage equalization (VE).**

NOMENCLATURE

MPP	Maximum power point.
TMPP	Total-minimum-power-point.
PBP	Power-balancing-point.
$V_{pv,i}$	Voltage of *i*th photovoltaic (PV) submodule.
$I_{pv,i}$	Current of *i*th PV submodule.
P_{total}	Total processed power in differential power processing (DPP) converters.
$P_{dpp,i}$	Power processed by *i*th DPP converter.
V_{eq}	Equalized voltage.
I_{string}	String current.
$I_{stringPBP}$	String current at PBP.
$I_{stringTMPP}$	String current at TMPP.
$I_{string,ref}$	Reference string current to proportional-integral (PI) controller.
P_{PBP}	Power at PBP.
$P_{PBP,worst}$	Worst-case power that one DPP converter needs to process using PBP control.
$P_{TMPP,worst}$	Worst-case power that one DPP converter needs to process using TMPP control.
$P_{single,max}$	The largest power for single DPP converter.
I_{mpp}	Current of a PV submodule at MPP.
$P_{loss,i}$	Power loss of the i^{th} DPP converter.
η_i	Efficiency of i^{th} DPP converter
η	Nominal efficiency of DPP converter
K	Set of DPP converters with negative current.
P	Set of DPP converters with positvie current.
k	Number of elements for set of K
p	Number of elements for set of P

Manuscript received September 24, 2018; revised July 15, 2019, October 3, 2019, January 6, 2020 accepted February 20, 2020. This work was supported by the National Natural Science Foundation of China (51977136), the Research development fund of XJTLU (RDF-16-01-10, RDF-17-01-28), the Research Enhancement fund of XJTLU (REF-17-01-02), the Suzhou Prospective Application programme (SYG201723), and the XJTLU Key Programme Special Fund (KSF-A-08, KSF-E-13, KSF-T-04).(Corresponding author: Huiqing Wen.)

G. Chu and H. Wen are with the Xi'an Jiaotong-Liverpool University, Suzhou 215123, China (e-mail: guanying.chu@xjtlu.edu.cn, huiqing.wen@xjtlu.edu.cn)

Y. Hu is with the University of York, York, YO10 5DD, U.K. (e-mail: yihua.hu@york.ac.uk)

L. Jiang is with the University of Liverpool, Liverpool, L69 3BX, U.K. (e-mail: l.jiang@liverpool.ac.uk).

Y. Yang is with the School of Rail Transportation, Soochow University. Suzhou 215131, China (e-mail: yangy1981@suda.edu.cn).

W. Wang is with the Suzhou Vocational University, Suzhou 215104, China (e-mail: wyiwang@163.com)

I. INTRODUCTION

Mismatches among photovoltaic (PV) elements such as cells or submodules caused by non-uniform aging, manufacturing tolerances, thermal gradients, partial shading, etc. are becoming one critical issue in maximizing the practical energy yield of PV systems [1]-[4]. The consequences of PV mismatches include loss of partial available power, hot spots, reliability, and lifespan reduction [4]. The research in [5] shows that the effects of mismatches among PV cell in the string will be high up to 30% in residential buildings. Although bypass diodes can be used to relieve the loss the output power, the mismatch-related losses are still high especially for the conventional central or string PV inverters since the total available power of one cell-string may be bypassed for a small-area shading [6], [7]. Furthermore, an additional problem caused by adding bypass diodes is the occurrence of multiple peaks in the power-voltage (*P-V*) curve, which requires a complicated algorithm to differentiate the global maximum power point (GMPP) from the local maximum power point (LMPPs) [8].

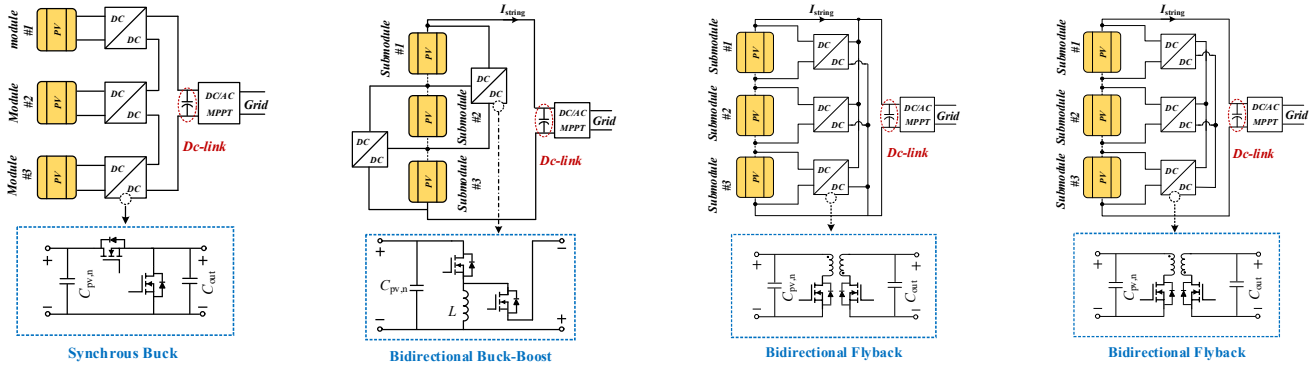

Fig. 1. Distributed PV architectures: (a) DC power optimizer; (b) PV-PV DPP architecture; (c) PV-bus DPP architecture; (d) PV-IP bus DPP architecture.

TABLE I
COMPARISON OF DIFFERENT DPP ARCHITECTURES

DPP architecture	Topology	Insolation	Relative amount of processed power	Voltage stress on switches	DPP control implementation	Converter independent control of PV submodule
PV-bus	Bidirectional Flyback [28], [31]-[33]	Yes	Low	$V_{pri}: V_{pv}$ $V_{sec}: V_{bus}$	90-92%	Yes
PV-IP bus	Bidirectional Flyback [34]-[37], [39]	Yes	Medium	$V_{pri}: V_{pv}$ V_{sec}: Variable	90%	No
PV-PV	Bidirectional Buck-boost [18, 22, 23, 26, 27] SC [24, 25]	No	High	$V_{pri}: 2\times V_{pv}$ $V_{sec}: 2\times V_{pv}$	88-92%	No

To address this issue, several distributed PV architectures have been proposed by implementing individual maximum power point tracking (MPPT) at the PV module or even submodule level. Fig. 1 illustrates the diagrams of several typical distributed power-electronics based PV architectures. Fig. 1(a) shows the diagram of the DC power optimizer (DCPO), which is a full-power-processing (FPP) based architecture to mitigate mismatches by paralleling a dedicated converter with each PV module with the realization of individual MPPT [9]-[17]. Specifically, the module-level DCPO has been discussed in [9]-[11], while the submodule-level DCPO has been presented [12]-[17]. As shown in Fig. 1(a), the synchronous-buck topology can be utilized as the converter to process the entire power generated by the PV elements. However, the power rating of the DC-DC converters should be set as high as the peak power rating of the PV module, which increases the hardware size and cost. All PV power goes through the converters. Thus, conversion losses are high. Since the system efficiency is highly dependent on the efficiency of DC-DC converters, the overall dc-stage system efficiency shown in Fig. 1(a) is limited according to the above power flow distribution analysis within the architecture of DCPO [18], [19].

To address these limitations of DCPO, a differential-power-processing (DPP) based PV architecture was introduced in [20] and [21]. DPP is a submodule-level architecture to process only the mismatching power among PV submodules, which is beneficial to reduce the power rating of DPP converters and improve system efficiency compared to the DCPO in FPP system [19]. For instance, the power process by DPP converter is zero or very small for the scenario with no or slight mismatches among PV submodules while FPP architecture must process the total power of the PV submodule. Consequently, both the hardware size and cost of power converters by using the DPP technique can be reduced, which facilitates the power integration design with the PV submodules or even PV cells. DPP architecture can be further classified into three connection configurations: PV-PV [18], [22]-[27], PV-bus [28]-[33], PV-to-isolated port bus (PV-IP bus) [34]-[39], as shown in Fig. 1(b), (c) and (d), respectively. A detailed comparison of three DPP architectures is presented in Table I. In PV-PV architecture, the number of DC-DC converters is always one less than PV elements. The possible converter topologies include the bidirectional buck-boost converter [18], [22], [23], [26], [27] or switch-capacitor (SC) converter [24], [25]. These topologies are all non-isolated topologies, which may bring electromagnetic interface (EMI) or safety issues. The individual MPPT can be achieved for each submodule-level DPP converter. Among three DPP architectures, the PV-PV architecture exhibits additional and compounded power processing when just one PV submodule is experiencing light or moderate mismatching. The main reason is that all DPP converters in the PV-PV architecture must participate in the power compensation even only one or several submodules are partially shaded [37]. This drawback will become more apparent for PV systems with a large number of PV submodules connected in series. For the PV-bus and PV-IP bus, it was reported that the DPP converters in PV-IP architecture process more than 33% of the power in the worst-case than the DPP converters in PV-bus architecture [28].

Meanwhile, the power processing ratio of the PV-bus architecture was found lowest among three architectures [36]. Furthermore, for the PV-bus architecture, the string current I_{string} is found independent on the operation point of the PV submodule, which means that maximum power point (MPP) operation can be realized for any value of I_{string}. Thus, the objectives of this paper are to improve the performance of PV-bus DPP in terms of conversion efficiency, system cost, and control complexity.

Control of PV-bus DPP architecture usually covers two levels: distributed submodule-level maximum MPPT control and simultaneously the centralized system-level control to adjust I_{string}. Specifically, due to the merits of isolation, high voltage gain and efficiency, bidirectional flyback converters (BFCs) are widely adopted as the DPP converters and connected in shunt to the PV submodules while the boost topology is used as the central converter to step up the string voltage to meet the AC-grid [31], [32]. Thus, classical MPPT methods such as perturb-and-observe (P&O) open-loop control by directly regulating duty cycles are used for BFCs, and the proportional-integral (PI) based closed-loop string current control is implemented for the boost converter. As for the power distribution within the PV-bus architecture, the boost converter will process the most generated power since its efficiency usually is higher than that of the isolated BFCs [33]. Moreover, the least power point tracking (LPPT) algorithm was proposed to find the optimal working point for I_{string} [31]. Although this real-time optimization algorithm shows effective in maximizing the power yield; however, it shows obvious limitations for the practical applications that can be summarized as follows:

1) ***High additional cost for accurate, current sensing and communication in DPP converters***: DPP architectures can be implemented at high granularity such as submodule or even level. With the individual P&O MPPT control, the module current and voltage must be measured in a real-time manner. Thus, the cost is high since every PV submodule requires the individual MPPT controller and sensors for module voltage and current measurement. Besides, communications among DPP converters will also add the system cost.

2) ***Uneven power stress among DPP converters***: the conventional LPPT may result in the power concentration on a single DPP converter due to complicated partial shading conditions (PSCs), which increase the power rating and cost of DPP converters.

3) ***Large oscillations in the output power***: these oscillations will result in extra energy losses, and they are mainly caused by the extremum-seeking algorithms. Specifically, the steady-state oscillations are caused by the LPPT algorithm, and the dynamic oscillations are generated by the perturbations of the MPPT algorithm and LPPT algorithm, as shown in Fig. 2.

4) ***High algorithm implementation complexity***: Since two extremum-seeking controls are implemented simultaneously, a well-coordinated implementation must be taken, especially the perturb steps. Specifically, multiple LPPT steps should be implemented within one MPPT step so that the string current can be regulated to the new steady-state optimal point. In an experimental test of [31], the MPPT perturbation step is increased to 10s to ensure a stable operation. This coordination will not only complicate the algorithm implementation but also lead to tracking failure under some fast-changing PSCs.

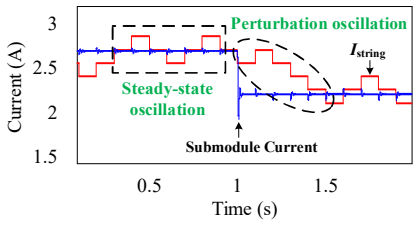

Fig. 2. Steady-state oscillation and perturbation oscillation.

To address the uneven power stress among DPP converters, a unit-minimum (UM) LPPT algorithm was proposed to realize even distribution the power stresses to DPP converters [32]. Compared with the LPPT algorithm, the UM-LPPT algorithm may result in higher total power processed by DPP converters [22], [40], [41]. Moreover, these issues of big oscillations, high complexity, and high-coupling in algorithm practical implementation still have not been solved.

Direct total-minimum-power-point (TMPP) control without perturbation introduced in [42] seems a promising solution for these limitations of the TMPP-based algorithm. Combing the merits of TMPP and power-balancing-point (PBP) algorithm, a low-complexity hybrid algorithm is proposed in this paper to find the most suitable operation point of I_{string} with low cost, small size, high system efficiency, and standardized modular design for DPP converters. Fig. 3 shows the circuit configuration and control diagrams. Specifically, simple submodule-level voltage equalization (VE) control is implemented to eliminate the expensive communication devices and relieve the control complexity while guaranteeing high tracking efficiency. For the system-level control, the proposed hybrid-algorithm is implemented to find the optimal string current accurately and quickly with less oscillation. Both simulation and experimental results under various scenarios are provided to validate the advantages of the proposed algorithm.

II. Effects of Mismatches and Voltage Equalization

In order to reduce the control overhead, a simple VE is introduced in the PV-bus DPP architecture for the submodule-level MPPT. An advantage of the VE control is that it can be implemented in a completely distributed manner without the need for communication among DPP converters. However, the effects of the simple VE on the MPPT efficiency under various working conditions should be carefully evaluated in terms of irradiance and temperature. Fig. 4(a) presents the circuit configuration for the PV output power versus voltage curves.

Considering that the temperature change is relatively small within one day, only the effect of the irradiance is considered in the experiments. In the test, a DC power supply RIGOL DP832 is connected with the selected 24-cell PV panel (PV-20 SFP2136) in parallel to emulate different irradiance conditions by injected different values of bias current. A programmable electronic load IT8514C+ is adopted to scan the output power versus voltage curve. The PV panel for the test has been used for three years so that the effect of PV aging can be covered in the test.

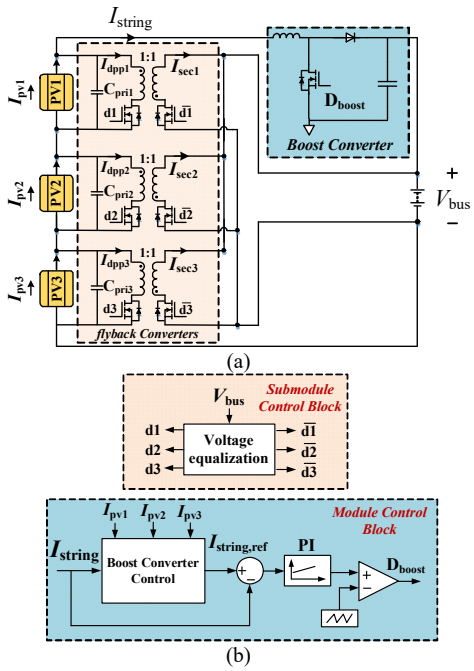

Fig. 3. (a) PV-bus DPP architecture. (b) Control block diagram for submodule level and module level.

The measured *P-V* curves under different irradiance conditions are illustrated in Fig. 4 (b). It should be noted that the measured MPP voltage change is 5.7% for an 80% irradiance variation, which is higher than the theoretical value of 4% due to the inclusion of the PV aging effect in the test. In the *P-V* curve, the absolute slope of the output power versus voltage is defined as $S=|dP/dV|$. Thus, three zones can be specified considering the value of S. Zone 2 shown in Fig. 4(b) is the focus of our research since all MPPs corresponding to different irradiance conditions are located in this region. It is worth noticing that the measured S in this region becomes flat, which indicates the output power is insensitive with the output voltage in this region. In Fig. 4(b), the star corresponds to the measured MPP for a specific irradiance value, and the dashed line represents the actual characteristic line with the simple VE control. Fig. 4(b) indicates that the difference between the actual output power with the VE control and the theoretical value is small although the location of MPP under the severe partial shading condition was found slightly deviated from the VE control line. Here the VE tracking efficiency is defined as

$$\sigma = \frac{P_{\text{VE,max}}}{P_{\text{MPPT,max}}} \tag{1}$$

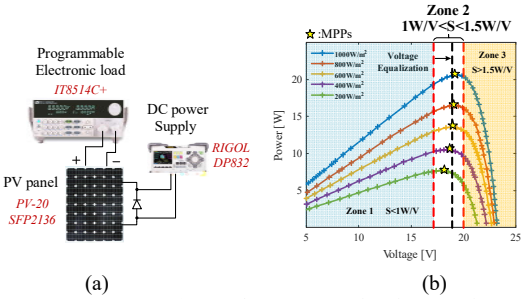

Fig. 4. PV output curve test: (a) Hardware connection for scanning P-V output curve; (b) Experimental P-V curve under different irradiances.

The calculated VE tracking efficiency is 99.3% under a severe partial shaded scenario with the irradiances set for two series-connected two PV panels as 1000W/m^2 and 200W/m^2, respectively. A complete tracking efficiency with the VE control is illustrated in Fig. 5, where the irradiance for PV submodule 1 is fixed at 1000W/m^2, the irradiance level for PV submodule 2 is changing from 100W/m^2 to 700W/m^2, and the irradiance level for PV submodule 3 is changing from 100W/m^2 to 900W/m^2. The changing step is set as 100W/m^2. Fig. 5 indicates that the average tracking efficiency is lower for higher irradiance differences. However, the measured lowest tracking efficiency is 98.8% for all the defined shading scenarios, which lays the solid basis for the implementation of the VE control, considering the significantly reduced cost and control complexity.

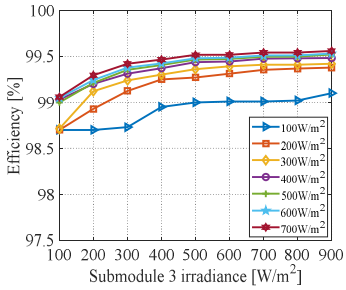

Fig. 5. Tracking efficiency with the VE method: submodule 1 is operating with full irradiance, the irradiance for submodule 2 is changing from 100W/m^2 to 700W/m^2 with the step of 100W/m^2, and the irradiance for submodule 3 is changing from 100W/m^2 to 900W/m^2 with the step of 100W/m^2.

III. Proposed Optimized Algorithm

A. *Total minimum power point (TMPP) control*

The PV-bus DPP architecture is controlled by the VE method so that each submodule is working at near the true MPP point. In order to minimize the total processed power of DPP converters, the string current I_{string} must be controlled to adjust the current flowing through DPP converters. The total power processed by n DPP converters in the PV-bus architecture can be expressed by:

$$P_{\text{total}} = \sum_{i=1}^{n} V_{\text{eq}} \left| I_{\text{pvi}} - I_{\text{string}} \right| \tag{2}$$

where n is the numbers of PV submodules, I_{pvi} is the current of i^{th} PV submodule, and I_{string} is the string current.

It is noted that the converter power flow is bidirectional and the processed power may be from the bus side to the PV submodule side or Versa. The power flow direction in (2) should be considered in building an accurate power loss model of the DPP converter considering the non-ideal effect. Then, (2) can be rewritten as:

$$P_{\text{total}} = \underbrace{\sum_{i\in P} V_{\text{eq}} \left(I_{\text{pvi}} - I_{\text{string}} \right)}_{\substack{\text{power from PV side to bus side} \\ I_{\text{pvi}} > I_{\text{string}}}} + \underbrace{\sum_{i\in K} \left[V_{\text{eq}} \left(I_{\text{string}} - I_{\text{pvi}} \right) + P_{\text{loss,i}} \right]}_{\substack{\text{power from bus side to PV side} \\ I_{\text{pvi}} < I_{\text{string}}}} \tag{3}$$

where P is the set of DPP converters with positive current, K is the set of DPP converters with negative current, and $P_{\text{loss,i}}$ is the power loss of i^{th} DPP converter in set of K, which can be expressed by:

$$P_{\text{loss,i}} \approx a\left(I_{\text{string}} - I_{\text{pvi}} \right)^2 + b\left(I_{\text{string}} - I_{\text{pvi}} \right) + c, \ \forall i \in K \tag{4}$$

where a, b, c are the weighting factors of the power loss model [43]. Then, the total processed power versus string current can be expressed as:

$$P_{\text{total}} = \underbrace{\sum_{i\in P} V_{\text{eq}}\left(I_{\text{pvi}} - I_{\text{string}}\right)}_{\substack{\text{power from PV side to bus side} \\ I_{\text{pvi}} > I_{\text{string}}}} + \underbrace{\sum_{i\in K}\left[V_{\text{eq}}\left(I_{\text{string}} - I_{\text{pvi}}\right) + \overbrace{a\left(I_{\text{string}} - I_{\text{pvi}}\right)^2 + b\left(I_{\text{string}} - I_{\text{pvi}}\right) + c}^{\text{Approximated losses}}\right]}_{\substack{\text{power from bus side to PV side} \\ I_{\text{pvi}} < I_{\text{string}}}} \quad (5)$$

Considering different conditions between the string current and the maximum PV submodule current, different cases can be separately discussed for the expression (5):

(1) **Case I** with "$I_{\text{string}} \geq \max\left\{i_{\text{pv1}}, i_{\text{pv1}} \ldots, i_{\text{pvn}}\right\}$": since I_{string} is larger than all the PV submodule current, the power direction of all DPP converters is always from the bus side to the PV submodule side, which means that $k = n$ for this case. Take $dP_{\text{total}}/dI_{\text{string}}$, then

$$\frac{dP_{\text{total}}}{dI_{\text{string}}} = kV_{\text{eq}} + 2a\left(kI_{\text{string}} - \sum_{i\in K} I_{\text{pvi}}\right) + bk \quad (6)$$

where k is the number of the elements in the set of K. Considering that the equalized voltage is positive, then, the slope in this interval is always positive for this case.

(2) **Case II** with "$I_{\text{string}} \leq \min\left\{i_{\text{pv1}}, i_{\text{pv1}} \ldots, i_{\text{pvn}}\right\}$": since I_{string} is smaller than all the PV submodule current, the power direction of all DPP converters is always from the bus side to the PV submodule side, which means that $p = n$ for this case. Take $dP_{\text{total}}/dI_{\text{string}}$, then

$$\frac{dP_{\text{total}}}{dI_{\text{string}}} = -P \times V_{\text{eq}} \quad (7)$$

(3) **Case III**: $\min\left\{i_{\text{pv1}}, i_{\text{pv1}} \ldots, i_{\text{pvn}}\right\} \leq I_{\text{string}} \leq \max\left\{i_{\text{pv1}}, i_{\text{pv1}} \ldots, i_{\text{pvn}}\right\}$, considering the string current is between the lowest and highest PV submodule current, take $dP_{\text{total}}/dI_{\text{string}}$, then:

$$\frac{dP_{\text{total}}}{dI_{\text{string}}} = V_{\text{eq}}\left(k - p\right) + 2a\left(kI_{\text{string}} - \sum_{i\in K} I_{\text{pvi}}\right) + bk \quad (8)$$

This case can be further discussed considering the possible value of "$k - p$":

A. $k - p > 0$: the slope expressed by (8) is always positive considering the equalized voltage V_{eq} and all weight factors are positive [43].

B. $k - p \leq 0$: the sign of the slope should be discussed as follows:

$$\begin{cases} if\ p - k < \dfrac{2a\left(kI_{\text{string}} - \sum_{i\in k} I_{\text{pvi}}\right) + bk}{V_{\text{eq}}}, & \dfrac{dP_{\text{total}}}{dI_{\text{string}}} < 0 \\ if\ p - k > \dfrac{2a\left(kI_{\text{string}} - \sum_{i\in k} I_{\text{pvi}}\right) + bk}{V_{\text{eq}}}, & \dfrac{dP_{\text{total}}}{dI_{\text{string}}} > 0 \end{cases} \quad (9)$$

The condition to achieve negative slope under this condition can be expressed by:

$$\max\left\{2a\left(kI_{\text{string}} - \sum_{i\in K} I_{\text{pvi}}\right) + bk\right\} \leq V_{\text{eq}},\ I_{\text{string}} \in \left[I_{\text{pvi}},\ I_{\text{pv},\frac{n+1}{2}}\right] \quad (10)$$

Considering the practical parameters for PV modules and power devices, the condition in (10) can be fulfilled, as explained in the Appendix. Thus, the slope of the total power versus the string current under Case III holds true. Thus, the optimal string current for the TMPP can be easily found among the possible submodule currents, namely $I_{\text{string}} \in \left\{i_{\text{pv1}}, i_{\text{pv1}} \ldots, \text{i}_{\text{pvn}}\right\}$. Meanwhile, the string current by using TMPP method is expressed as:

$$I_{\text{stringTMPP}} = \underbrace{\arg\min}_{I_{\text{s}} \in \left\{i_{\text{pv1}}, i_{\text{pv2}} \ldots, i_{\text{pv3}}\right\}} \left\{\sum_{i=1}^{n} V_{\text{eq}}\left|I_{\text{pvi}} - I_{\text{s}}\right|\right\} \quad (11)$$

Fig. 6 shows the difference of the total processed power for DPP converters by considering the non-ideal effect such as power loss. The red curve shows the built accurate model with the non-ideal effect, while the blue curve represents the ideal model without considering the non-ideal effect. With the consideration of the practical power loss, the total processed power of the non-ideal model is larger than that with the ideal since the power loss is considered. Moreover, the power difference becomes larger with the increase of the string current. However, expression (11) still holds true. Furthermore, for different numbers of PV submodules, the optimal I_{string} by using the TMPP can be expressed by:

$$\text{TMPP}\begin{cases} I_{\text{string}} = I_{\text{pv},\frac{n+1}{2}} & \text{when n is odd} \\ I_{\text{string}} \in \left[I_{\text{pv},\frac{n}{2}}, I_{\text{pv},\frac{n}{2}+1}\right] & \text{when n is even} \end{cases} \quad (12)$$

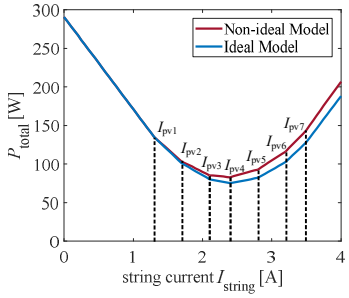

Fig. 6. Comparison of the total processed power versus the string current by using a non-ideal model and ideal model.

B. Power balancing point (PBP) control

Another important issue for the PV-bus DPP system is the power stress of DPP converters since the ideal TMPP control will easily result in the uneven power distribution among DPP converters under some PSCs. Specifically, based on the modular design concept, the theoretical power rating of DPP converters with the TMPP should be set as the maximum output power of PV submodules, which adds the system cost. Furthermore, the uneven power distribution will affect the system lifetime and reliability due to the potential risks posed by the heavily loaded DPP converter. Thus, the PBP control is presented here.

Consider that a practical PV module usually consists of 60 or 72 solar cells, which can be usually divided into two or three submodules. In this work, a three-submodules case will be

TABLE II

POWER DISTRIBUTION FOR THREE-SUBMODULE PV-BUS SYSTEM

Condition	P_{total}	P_{dpp1}	P_{dpp2}	P_{dpp3}
$I_{string} \leqslant I_{pv1} < I_{pv2} < I_{pv3}$	$V_{eq}(I_{pv1}+I_{pv2}+I_{pv3}-3I_{string})$	$V_{eq}(I_{pv1}-I_{string})$	$V_{eq}(I_{pv2}-I_{string})$	$V_{eq}(I_{pv3}-I_{string})$
$I_{pv1} \leqslant I_{string} < I_{pv2} < I_{pv3}$	$V_{eq}\left(I_{pv2}+I_{pv3}-I_{pv1}-I_{string}\right)$	$V_{eq}\left(I_{string}-I_{pv1}\right)$	$V_{eq}(I_{pv2}-I_{string})$	$V_{eq}\left(I_{pv3}-I_{string}\right)$
$I_{pv1} < I_{pv2} \leqslant I_{string} < I_{pv3}$	$V_{eq}\left(I_{pv3}-I_{pv2}-I_{pv1}+I_{string}\right)$	$V_{eq}\left(I_{string}-I_{pv1}\right)$	$V_{eq}\left(I_{string}-I_{pv2}\right)$	$V_{eq}\left(I_{pv3}-I_{string}\right)$
$I_{pv1} < I_{pv2} < I_{pv3} \leqslant I_{string}$	$V_{eq}\left(3I_{string}-I_{pv1}-I_{pv2}-I_{pv3}\right)$	$V_{eq}\left(I_{string}-I_{pv1}\right)$	$V_{eq}\left(I_{string}-I_{pv2}\right)$	$V_{eq}\left(I_{string}-I_{pv3}\right)$

discussed to present the difference between PBP and TMPP. Then, a generalized N-submodule case will be discussed to derive the general equation.

1) Three submodules case

For the three-submodule based DPP system, analysis can be made according to the distribution of the string current. Table II summarizes the expressions of the total power processed by three DPP converters P_{total}, and the power for each DPP converter $P_{dppi(i=1,2,3)}$ for different conditions.

For the three-submodule based PV-bus DPP system, the distribution of P_{total} and $P_{dppi(i=1,\,2,\,3)}$ with respect to the string current by using the TMPP and PBP is illustrated in Fig. 7. Specifically, when "$I_{string} \leqslant I_{pv1} < I_{pv2} < I_{pv3}$", the slopes for "$P_{total}$, P_{dpp1}, P_{dpp2}, P_{dpp3}" are "-3, -1, -1, -1". The corresponding slopes for other regions can be obtained as: "-1, 1, -1, -1" when "$I_{pv1} \leqslant I_{string} < I_{pv2} < I_{pv3}$", "1, 1, 1, -1" when "$I_{pv1} < I_{pv2} \leqslant I_{string} < I_{pv3}$", and "1, 1, 1, 1" when "$I_{pv1} < I_{pv2} < I_{pv3} \leqslant I_{string}$". With the TMPP control, the point G can be detected with the slope of P_{total} changing from "-1" to "1". However, the power stress distribution among three DPP converters is obviously uneven. The power processed by the second DPP converter is zero, while two-thirds of P_{total} will be exerted on the first DPP converter, which will result in a high-power rating for all DPP converters considering the modular design concept. To reduce the system cost and improve the lifetime, a new working point F should be selected considering both requirements of low system processed power and even power distribution. The black dash line indicates the PBP.

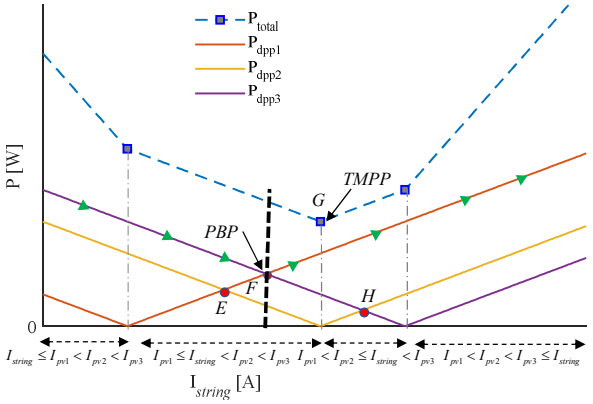

Fig. 7. Power distribution comparison of two controls for three-submodule based DPP system: TMPP and PBP.

2) Generalized N-submodule Case

The above analysis is effective for three PV submodules. The power distribution and power stress analysis can be easily extended to a generalized N-submodule case.

Here, the PBP control for a generalized PV-bus DPP architecture with N submodules is presented. With the VE control, each PV submodule exhibits the same output voltage, thus $V_{eq} = V_{pv1} = V_{pv2} = \ldots V_{pvn}$. Assume the output current of PV submodules meet the relationship of "$I_{pv1} < I_{pv2} \ldots < I_{pvn}$", where the I_{pv1}, I_{pv2}, and I_{pvn} represent the output current of PV submodules. The general form for the power processed by each DPP converter is expressed by:

$$P_{dppi} = \begin{cases} V_{eq}\left(I_{pvi} - I_{string}\right) & I_{string} < I_{pvi} \\ \dfrac{V_{eq}\left(I_{string} - I_{pvi}\right)}{\eta_i} & I_{string} > I_{pvi} \end{cases} \tag{13}$$

Equation (13) indicates that the curve slope of $P_{dppi}(i=1\ldots n)$ with respect to the string current will change from "-1" to "1" with the increase of the string current. Moreover, the point PBP is found always the intersection between the curve of P_{dpp1} and P_{dppn}. Thus, the balancing power P_{PBP} can be expressed by:

$$P_{PBP} = \frac{V_{eq}\left(I_{string} - I_{pv1}\right)}{\eta_1} = V_{eq}\left(I_{pvn} - I_{string}\right) \tag{14}$$

Here, in order to yield a more intuitive closed form expression for the generalized N-submodule based PBP control, an approximation is made to set the efficiencies of all DPP converters approximately equal to the designed nominal conversion efficiency across the entire specified load range that $\eta \backsimeq \eta_i$ considering a relative small manufacturing tolerance [44]. Then, the expression of the string current at PBP for the PV-bus DPP architecture with N submodules can be derived as:

$$I_{stringPBP} = \frac{I_{pv1} + \eta I_{pvn}}{1+\eta} \tag{15}$$

where I_{pv1} is the minimum submodule current, I_{pvn} is the maximum submodule current, and η_1 is the conversion efficiency of DPP converter 1, which corresponds to the lowest current PV submodule. It can be found that $I_{stringPBP}$ is mainly determined by the maximum submodule current and the minimum submodule current in the system.

Substitute (15) into (14), the power stress of the DPP converter by using PBP control can be expressed by:

$$P_{PBP} = V_{eq}\frac{\eta\left(I_{pvn} - I_{pv1}\right)}{1+\eta} \tag{16}$$

Thus, the worst-case power that one DPP converter needs to process is expressed by:

$$P_{\text{PBP,worst}} = \frac{V_{\text{eq}} I_{\text{pvn}}}{1+\eta} \tag{17}$$

For the comparison, the corresponding worst-case power for one DPP converter by using TMPP method is expressed by:

$$P_{\text{TMPP,worst}} = \frac{V_{\text{eq}} I_{\text{pvn}}}{\eta} \tag{18}$$

The above analysis indicates that PBP control can reduce the power rating of DPP converters to nearly half of that with conventional TMPP-based control under the worst PSC condition considering that the nominal efficiency of the DPP converter is usually more than 90%.

C. *Error Analysis*

Equation (15) indicates that the string current corresponding to the PBP is dependent on the efficiency by using the non-ideal model. However, with the ideal model, the PBP current should be located at the middle point between two extreme submodule currents. Here, the error of the optimal string current by using the between the ideal model and the non-ideal model is analyzed, which corresponds to the scenario in three-submodule based PV-bus architecture with one PV submodule fully shaded and the other two fully illuminated. The range of efficiency for BFCs is 84%-92%, and the MPP current under STC is 1.1A. The calculated errors with respect to the efficiency and PV submodule current are presented in Fig. 8. It is noted that the maximum error is limited below 0.05A, which is negligible for practical design. Therefore, the middle value of two extreme submodule currents will be adopted as the optimal PBP current for the practical implementation.

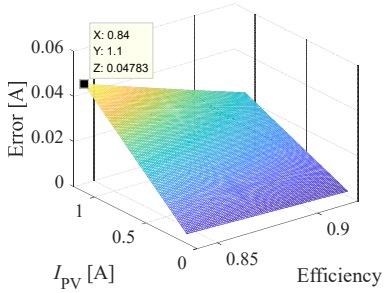

Fig. 8. Error analysis by considering the non-ideal factors such as the practical efficiency.

D. *Proposed Algorithm*

For an *N*-submodule PV system, the possible output power of each PV submodule will change from zero to its maximum output power. The implementation of the proposed PBP based optimization algorithm should consider different cases. Here three cases are separately discussed with the string current regulated at bypass, TMPP, and PBP mode. Case one is defined that PV cells in one submodule are fully shaded. The boundary is defined by whether the output current of the PV submodule is larger than 0.1A. For this case, the shaded submodule will not generate any power while the power processed by the corresponding DPP converter will be expressed by

$$P_{\text{dppi}} = \frac{V_{\text{eq}} I_{\text{string}}}{\eta} \tag{19}$$

Thus, bypass mode is required to shut off the full-shaded PV submodule to reduce the total processed power. Fig. 9. Effects of the bypass mode when one PV submodule is completely shaded. The irradiation on three submodules are set as: 0W/m^2, 500W/m^2, and 1000W/m^2, respectively. With the bypass mode, the total power and power proceeded by each DPP converter will cut to half while the energy harvest from the PV system will maintain unchanged.

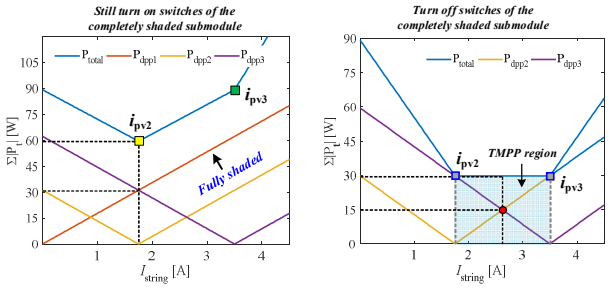

(a) (b)

Fig. 9. Effects of the bypass mode when one PV submodule is completely shaded. (a) Without bypass mode. (b) With bypass mode.

Fig. 10 illustrates the operations for the bypass mode. Once the current sensor detects that the output current of one submodule is less than 0.1A, the power devices of the DPP converter are turned off while the bypass diode is active. The bypass mode can effectively reduce the total power as well as reducing the power stress on every single DPP converter.

The selection between the TMPP and PBP mode lies in the actual output of each DPP converter. If any output power is found less than the defined boundary in (17), the TMPP mode will be implemented to reduce the total power loss. Otherwise, the PBP mode is implemented to make the power stress distribution even while reducing the whole processed power. Fig. 11 illustrates the flowchart of the proposed algorithm.

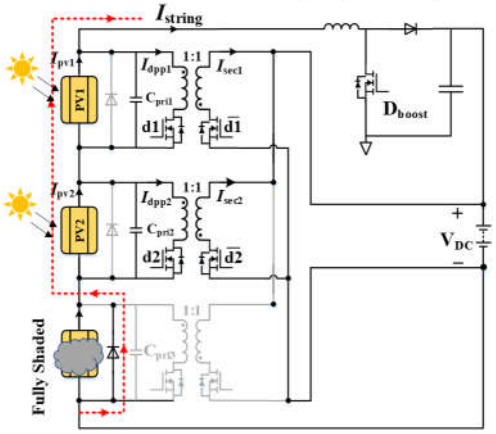

Fig. 10. Bypass mode when some submodules are heavily shaded.

IV. Simulation Evaluation

In order to validate the proposed algorithm, a simulation test was built in PSIM. The PV panel model is MSX60W, and the specifications are shown in Table III. In the simulation evaluation, the power loss of DPP converters are ignored. The

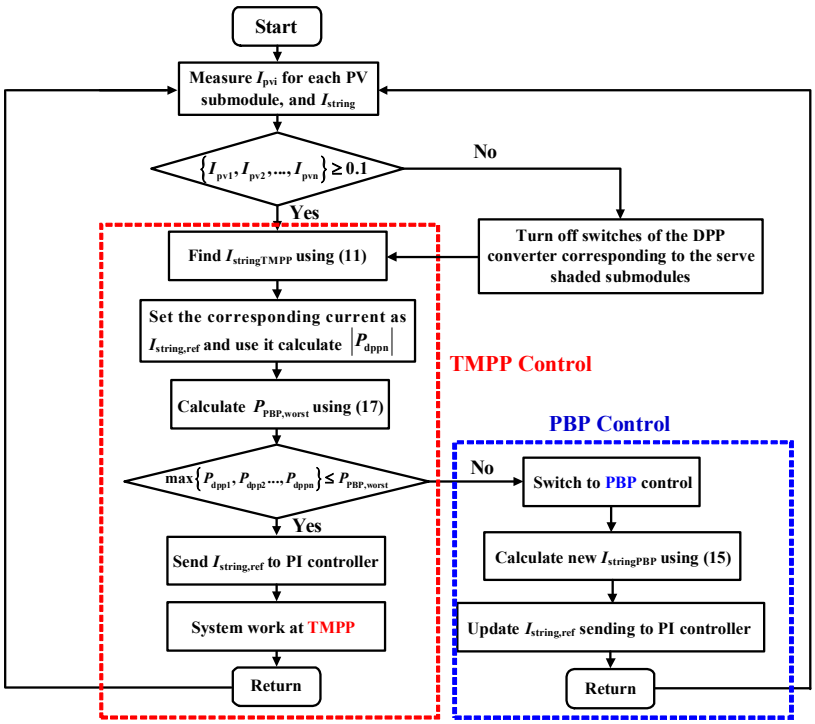

Fig. 11. Flow chart of the proposed algorithm.

irradiances for two submodules are set as 600W/m^2 and 1000W/m^2, respectively. The corresponding MPP parameters for two submodules are: $V_{mpp,pv1}$ = 17V, $I_{mpp,pv1}$ = 2.13A and $V_{mpp,pv2}$ = 17.1V, $I_{mpp,pv2}$ = 3.5A. With the voltage equalization, the voltage for two submodules should be regulated at: V_{eq} = ($V_{mpp,pv1}$+$V_{mpp,pv2}$)/2 = 17.05V, meanwhile, the corresponding equalization current is I_{pv1} ≈ 2.13A and I_{pv2} ≈ 3.5A. The PBP value is calculated as 2.835A.

TABLE III
SPECIFICATION OF PV PANEL MSX60W

Parameter	Symbol	Value	Parameter	Symbol	Value
Number of cells	N_s	36	Maximum Power (W)	P_{mpp}	60
Voltage at MPP (V)	V_{mpp}	17.1	Current at MPP (A)	I_{mpp}	3.5
Open-circuit voltage (V)	V_{oc}	21.1	Short-circuit current (A)	I_{sc}	3.8
Temperature Coeff. Of V_{oc}	*NA*	-0.38	Temperature Coeff. Of I_{sc}	*NA*	0.065
Band Energy (eV)	E_g	1.12	Ideality Factor	*NA*	1.2
Shunt Energy (Ω)	R_p	1000	Series Resistance (Ω)	R_s	0.008

A. Voltage equalization algorithm

Fig. 12 shows the main simulation results with the VE control. The output voltages of two submodules are regulated to the same value due to the VE control, as shown in Fig. 12(a). The output currents of the two submodules are distinct due to the different excreted irradiances. With the LPPT, the optimal string current can be obtained, which is labeled as $I_{string,ref}$. which is 2.835A. The actual string current will be regulated around the reference, as illustrated in Fig. 12(c). The output power absolute value of each DPP converter is illustrated in Fig. 12(d), which indicates that the powers processed by two DPP converters share the same absolute value while totally different polarity. Specifically, DPP1 will extract power from the submodule 1 while DPP2 will inject power to the submodule 2.

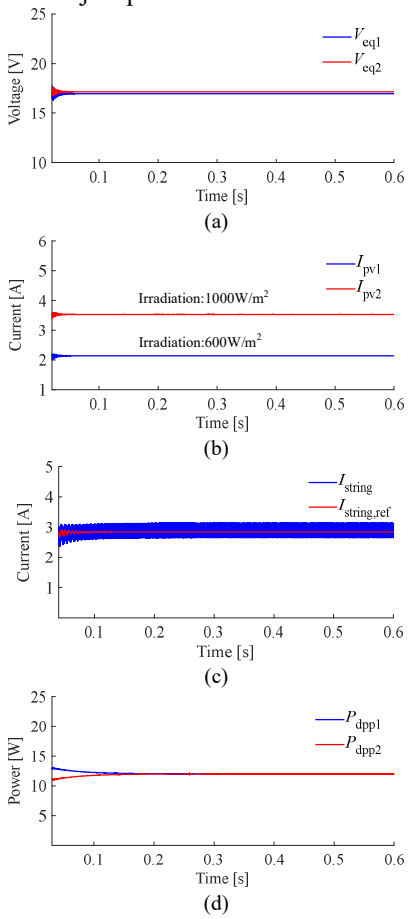

TABLE IV
COMPARATIVE RESULTS OF SEVERAL SHADING SCENARIOS UNDER DIFFERENT WORKING POINTS

Shading Scenario	I_{pv1}	I_{pv2}	I_{pv3}	Total processed power (TMPP)	Power Distribution	Total processed power (PBP)	Power Distribution	Mode Selection
Case #1	3.55A	3A	0.4A	53.55W	P_{dpp1}=9.35W P_{dpp2}=0W P_{dpp3}=44.2W	70.97W	P_{dpp1}=26.77W P_{dpp2}=19.91W P_{dpp3}=26.77W	PBP
Case #2	3.55A	3.2A	0A	60.35W	P_{dpp1}=5.95W P_{dpp2}=0W P_{dpp3}=54.4W	84.57W	P_{dpp1}=30.17W P_{dpp2}=24.23W P_{dpp3}=30.17W	PBP
Case #3	1.5A	1.5A	0A	25.5W	P_{dpp1}=0W P_{dpp2}=0W P_{dpp3}=25.5W	38.25W	P_{dpp1}=12.75W P_{dpp2}=12.75W P_{dpp3}=12.75W	TMPP
Case #4	3A	3A	1.7A	22.1W	P_{dpp1}=0W P_{dpp2}=0W P_{dpp3}=22.1W	33.15W	P_{dpp1}=11.05W P_{dpp2}=11.05W P_{dpp3}=11.05W	TMPP

Fig. 12. VE for the steady-state. (a) Submodules output voltage; (b) Submodules output current; (c) String currents of the boost converter; (d) Power processed by each DPP converter with DPP1 extracting power and DPP2 injecting power from the corresponding submodule.

Fig. 13 illustrates the simulated results under the irradiance changing condition, which is defined in Fig. 13(a). Specifically, the irradiation on the submodule 1 first decreases from 1000W/m^2 to 800W/m^2 and then decreases to 500W/m^2, at t *=0.3s* and t *= 0.6s,* respectively. Similarly, for submodule 2, the irradiance decreases from 700W/m^2 to 300W/m^2 and then increases to 1000W/m^2. Fig. 13 (b) presents the output current of each submodule using the VE control. Fig. 13 (c) indicates that the string current with the VE control follows the reference with high accuracy and speed under different conditions. Although the discrepancies in the power curve by each DPP converter exist for a short period time, as shown in Fig. 13(d), two curves quickly converge to the same output power value with the VE-based LPPT control.

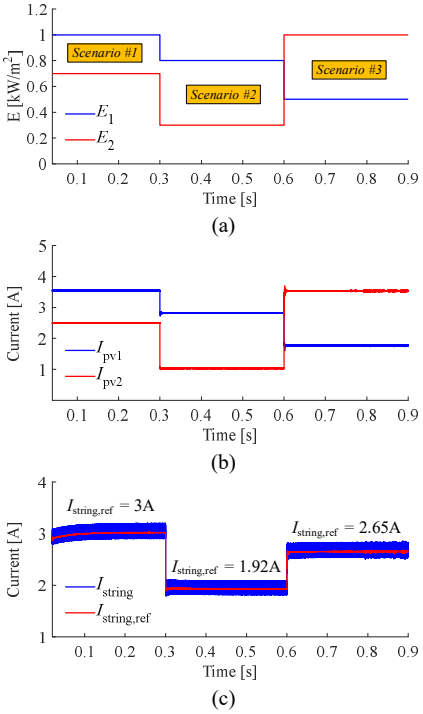

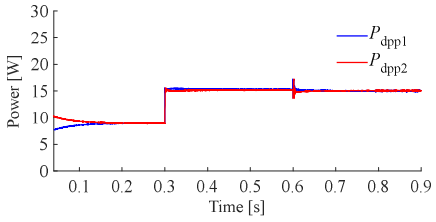

(d)

Fig. 13. VE for the dynamic test. (a) Irradiation changing pattern; (b) Submodules output current; (c) String currents of the boost converter; (d) Power processed by each DPP converter.

B. TMPP versus PBP

TMPP is preferable in improving the system efficiency while the PBP can realize the even distribution of power stress among DPP converters, which is important for the standardized modular design. Theoretically, the maximum power stress that one DPP converter will withstand is the MPP power of the PV submodule. Specifically, for the MSX60W PV panel, the power stress of the DPP converter reaches to 60W using TMPP control under the worst shading case, which corresponds to the scenario when one submodule is fully shaded while the other two submodules are fully irradiated. However, the worst-case power that one DPP converter needs to proceed is 30W by using PBP, which indicates that the power rating with PBP control can be reduced by 50% compared to that with TMPPT control. Here the power rating of DPP converters is set as 35W considering some design margin. Table IV shows the power distributions for different shading conditions. It shows that DPP3 has the largest power stress in most cases by using TMPPT control. Especially for case 2, DPP3 proceeds 90% of the total power, which will result in a higher operating temperature of DPP3 than other DPP converters, as shown in Fig. 14(a). Higher temperatures will result in a high failure rate of switching devices such as MOSFETs [45]. Consequently, the mean time between failure (MTBF) of DPP3 is affected [46]. Thus, it is important to implement the PBP control in order to balance the power stress and achieve the even distribution of working temperature among DPP converters. Fig. 14(b) shows the temperature distribution using the PBP control, which indicates that the even distribution of the working temperature has been achieved. As illustrated in Table IV, with PBP, the maximum power stress of DPP converters can be reduced to about 30W, which is a 50% reduction compared with the TMPP control. Fig. 15 presents the

comparison of the whole power and maximum power stress by using two controls, where TMPP-P_{total} and PBP-P_{total} represent the whole power by two controls or modes. TMPP-$P_{\text{single-max}}$ and PBP-$P_{\text{single-max}}$ represent the maximum power stress by two modes. It shows that power stress can be reduced significantly while the increase of the total power is large, namely about 32% and 40% for cases #1 and #2, respectively. Thus, it is necessary to switch the mode between the TMPP and PBP according to the actual output power of each DPP converter.

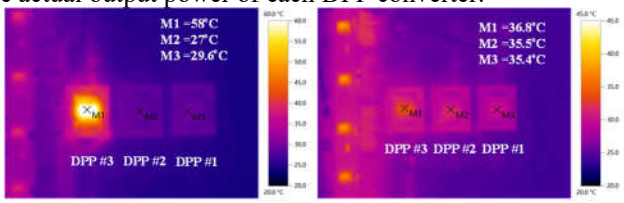

(a) (b)

Fig. 14. Comparison of temperature distribution measured by the thermal imager under case #2 for different control methods. (a) TMPP. (b) PBP.

As illustrated in the algorithm flowchart in Fig. 11, the output power of each DPP converter should be monitored to switch the operation mode. Once the output power of each DPP converter is less than the set boundary, the TMPP is implemented. Otherwise, the PBP is used to make the power distribution even. For the shading cases, #3 and #4 in Table IV, the maximum power-stress on one certain DPP converter is less than the power rating value (all the blue columns is lower than the blue dotted line) as shown in Fig. 15(a). Neither TMPPT nor PBP will not exceed the set power rating. However, it can be seen from Fig. 15(b) that the total power processed by the converter when using PBP is more than the total power processed by the converter when using TMPP. Furthermore, the conversion efficiencies of the bidirectional flyback converter and centralized boost converter are illustrated in Fig. 16(a) and (b), respectively. Fig. 16(c) shows the calculated power loss using TMPP and PBP four shading cases, which indicates that TMPP can reduce the total loss of DPP converters compare to PBP. Therefore, these results validate the correctness of the proposed algorithm in the selection of operation modes.

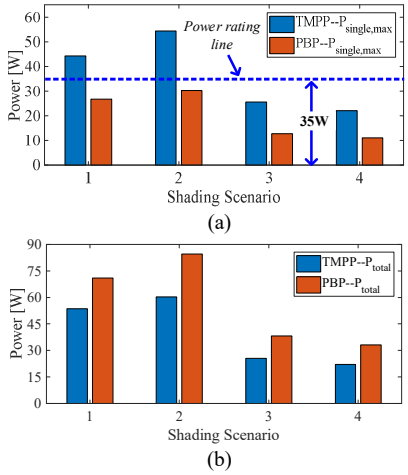

Fig. 15. Comparison of the power stress and total proceeded power with TMPP and PBP mode: (a) Maximum power stress by using TMPP and PBP. (b) Total processed power with TMPP and PBP.

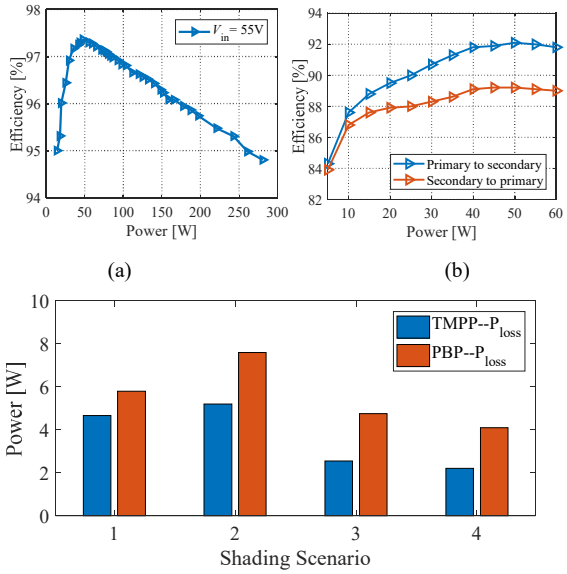

Fig. 16. (a) BFC efficiency. (b) Centralized boost converter efficiency. (c) Power loss comparison using different control methods under the specific partial shading scenario.

C. *Whole algorithm evaluation*

Fig .17(a) defines the change of partial shading. Specifically, the irradiation on the submodule 1 firstly increases from 800W/m^2 to 1000W/m^2 at t =*0.3s* and then decreases to 900W/m^2 and t = *0.6s*. For submodule 2, the irradiance decreases from 600W/m^2 to 300W/m^2 and then increases to 500W/m^2. For submodule 3, the irradiance decreases from 400W/m^2 to 200W/m^2 and then decreases to 0W/m^2. According to the irradiance change conditions, three scenarios can be classified. Fig. 17 illustrates the main simulation results under the three scenarios with the proposed algorithm. As shown in Fig. 17(b), the output voltage of three submodules is equal under scenario #1 and scenario #2 due to the VE control. Under scenarios #3, since the irradiance of submodule 3 is 0W/m^2 (completely shaded), the bypass mode is implemented, and the switches of the corresponding DPP converter are off. Thus, the voltage of submodule 3 is close to 0V, while the voltages of the other two submodules remain unchanged. The output currents of each submodule are shown in Fig. 17(c). Under scenario #1, the optimal string current value by using the TMPP control is 2.12A, then the powers processed by each DPP converter can be calculated as $\{P_{\text{dpp1}} = 12.3\text{W}, P_{\text{dpp2}} = 12.3\text{W}, P_{\text{dpp3}} = 0\text{W}\}$, which are lower than the defined power stress boundary 35W. Therefore, the string current in scenario #1 works at TMPP to ensure DPP converters process the minimum power. Under scenario #2, the optimal string current value by using the TMPP control is 1.03A, then the powers processed by each DPP converter can be obtained as: $\{P_{\text{dpp1}} = 43\text{W}, P_{\text{dpp2}} = 0\text{W}, P_{\text{dpp3}} = 5.6\text{W}\}$. Since the power flows through DPP1 is larger than the defined boundary, the proposed algorithm switches the mode from TMPP to PBP. Under scenario #3, since the submodule 3 is completely shaded without output power harvest, the switches of the corresponding DPP converter are turned off, and the bypass mode is activated to improve the system efficiency. Then, the system switches to the two-submodule PV-bus architecture and the string current always works at PBP mode for two-

submodule DPP architecture according to the discussion as mentioned above. Fig. 17(d) and (e) validate the control mode change and the corresponding transition speed. Specifically, under scenario #1, the string current works at TMPP with value 2.12A, and DPP1 and DPP2 process power 12.3W, respectively. Under scenario #2, the string current works at the PBP with value 2.11A; meanwhile, the powers processed by each DPP converter are 24.5W, 24.5W, and 18.5W, respectively. Under scenario #3, the string current works at the PBP with value 2.48A, and the power processed by DPP1 and DPP2 is the same 12.2W. Meanwhile, DPP 3 does not process any power.

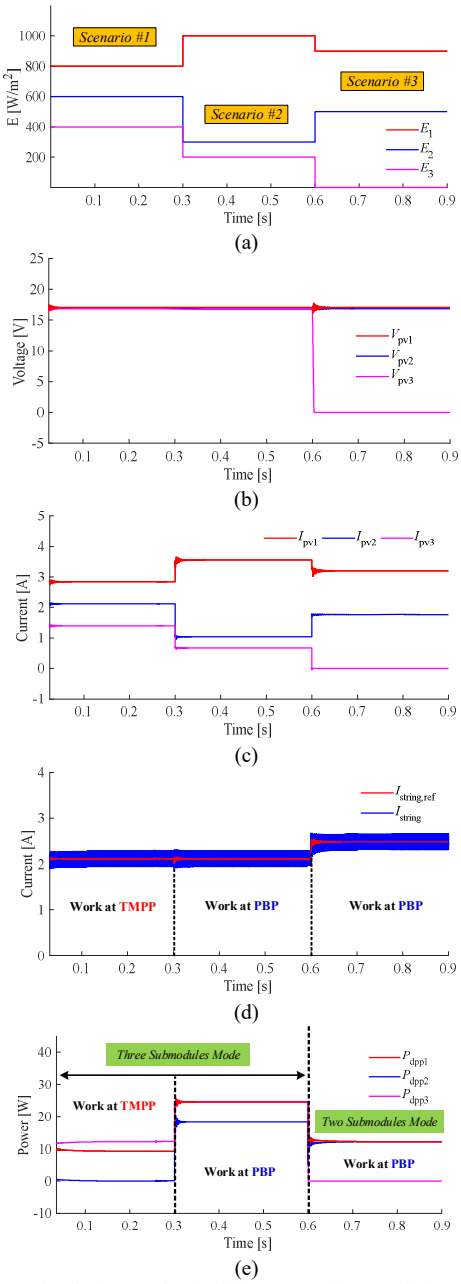

Fig. 17. PSIM simulation results for different working conditions. (a) Irradiation changing pattern; (b) Submodules output voltage using VE; (c) Submodules output current using VE; (d) String currents of the string boost converter; (e) Power processed by each DPP converter.

D. *Effect of DC-link Capacitance*

As shown in Fig. 3, the output of DPP converters in PV-bus architecture is connected in parallel with the DC link, which is usually regulated within a set range [47]. Here, in order to evaluate the effect of dc-link capacitance on the proposed algorithm, a dc-link capacitor parallel with the load resistor is used for the simulation evaluation.

For the simulation, the PV submodule 1 and 2 are assumed to receive uniform irradiation 1000W/m^2 while PV submodule 3 is partially shaded. Specifically, the dynamic irradiance changes for PV submodule 3 is set from 500W/m^2 to 800W/m^2 at $\boldsymbol{t = 1}$**s**. The simulated results of the total processed power of the DPP converter and bus voltage with respect to the dc-link capacitance are shown in Fig. 18(a) and (b), respectively. Fig. 18(a) shows that the total processed power by DPP converters is dynamically changing with respect to the irradiation-changing conditions, which verified the effectiveness of the proposed control for various operating conditions. With the change of the irradiation conditions, the variation of the dc-link voltage is small, specifically 5V in Fig. 18(b). Although the dynamic transient period show difference with respect to the dc-link capacitance, the transient time is short. Moreover, the effectiveness of the proposed PBP control still holds true because it mainly focuses on steady-state optimization.

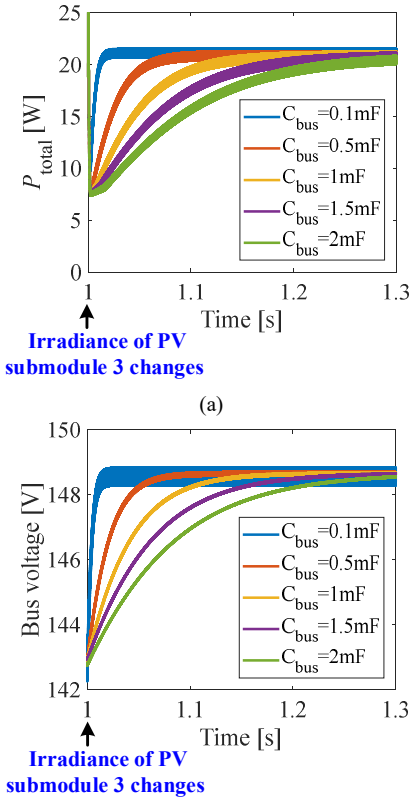

Fig. 18. Effect of dc-link capacitance. (a) Total processed power by DPP converters; (b) Voltage of dc-link capacitance.

V. Experimental Results

A. *Prototype*

In the experimental test, the experimental test bench and PCB hardware are shown in Fig. 19(a) and (b), respectively. Totally three submodule BFCs and one centralized boost converter are

designed in the PCB, as shown in Fig. 19 (b). Each PV submodule is equipped with a BFC to achieve the VE control. The centralized boost converter is utilized to implement the hybrid algorithm so that I_{string} is adjusted in real-time, and all the generated power from PV submodules can be processed. The maximum power stress of BFCs by using PBP control is calculated around 10W, which is set as the power rating of BFCs. The switching device the as IRF740, and the switching frequency is 100 kHz. The transformer was designed with 10 turns of 18# Litz wire on the primary and secondary considering the skin effect and proximity effect losses of using Litz wires for high-frequency applications. The magnetic inductance was 50μH, and the leakage inductance was set as 230nH. The main circuit parameters of BFC are shown in Table V.

TABLE V
PARAMETERS OF THE FLYBACK CONVERTER PROTOTYPE

Item	Parameter
Input voltage	4-21V
Switching frequency	100kHz
MOSFET	IRF740
Transformer turn ratio	1:1
Magnetizing inductance	50μH
Power rating	10W
Capacitor	240μF × 6
Converter peak Efficiency	92%

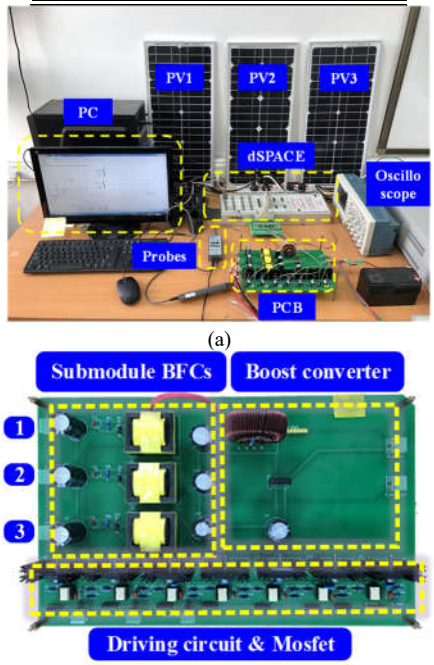

(a)

(b)

Fig. 19. Photograph of indoor experimental tests. (a) Experimental test bench. (b) PCB hardware.

B. Indoor experimental test

The indoor test was firstly conducted since the irradiance can be accurately regulated. In the test, each submodule was connected in parallel with the RIGOL DP832 DC power supply and the constant-current (CC) mode of the dc power supply was used. Thus, the photo-diode generated current will be emulated by the output current from DC power supply, and various irradiance changing conditions can be considered in the experimental evaluation, as shown in Fig. 20. Fig. 21 presents the measured *P-V* and *I-V* characteristic curve of PV-20 SFP2136.

Fig. 20. Experimental connection to emulate different irradiance conditions.

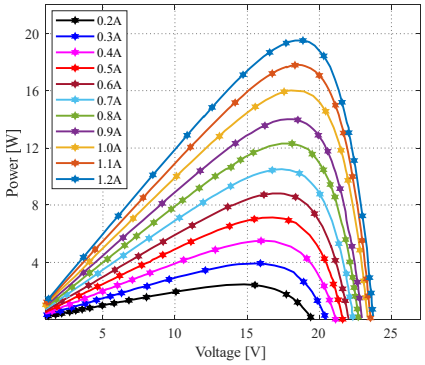

Fig. 21. Measured output characteristics for PV-20 SFP2136.

During the test, the control algorithm was implemented by dSPACE DS-1104, which is a real-time controller for power electronics. The execution time of the proposed algorithm in dSPACE was recorded as 5.186ms. Other digital controllers, such as DSP or low-cost microprocessors, can also be used to implement the algorithm [31]. The experimental objective is to verify the tracking accuracy and speed of the proposed control. A partial shading pattern is defined and applied in the experiments. Specifically, submodule 2 and 3 are partially shaded while the rest of submodule 1 receive uniform irradiance of 1kW/m^2. As shown in Fig. 22, the irradiation on the submodule 2 first decreases from 1000W/m^2 to 700W/m^2 and then decreases to 350W/m^2, at t_1 and t_2, respectively. Similarly, for submodule 3, the irradiance increases from 250W/m^2 to 350W/m^2 and then decreases to 0W/m^2.

Based on different partial shading patterns, the experimental results are shown in Fig. 23. The TMPP for the first partial shading pattern is 1.1A. However, the power processed by the DPP3 converter is 14.45W, which is exceeding the power rating of 10W. Therefore, the string current by using the PBP control is 0.7A under the first partial shading pattern, as shown in Fig. 23(a). The TMPP for the second partial shading is 0.9A, and the power consumed by the three converters is less than the power rating. Therefore, the string current operates at the TMPP under the second partial shading pattern, as shown in Fig. 23(b). The irradiation on the submodule 3 decreases to 0W/m^2 at t_2. Meanwhile, the proposed algorithm will turn off the switches of the DPP converters switching the system to two submodules mode. Therefore, the string current works at PBP with value 0.75A under the third partial shading pattern. The measured system efficiencies under the three shading patterns by using TMPP and PBP control strategy are shown in Table VI,

respectively. It can be seen that the system presents a higher efficiency by using TMPP control strategy since the DPP converters process less power. However, the PBP control should be used when the maximum power stress of any DPP converter is observed higher than the designed power rating, as shown in the first and second shading conditions. Therefore, the proposed hybrid-algorithm can reach a good balance between efficiency and power stress. Specifically, the proposed hybrid-algorithm not only ensures high system efficiency but also reduces the power stress of DPP converters with respect to the set power rating.

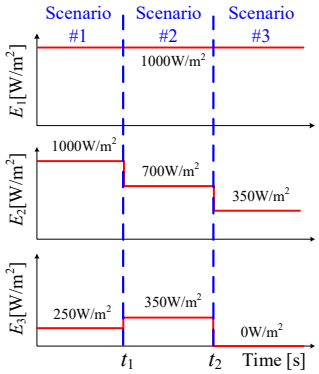

Fig. 22. Definition of partial shading patterns for three submodules: submodule 1, submodule 2, and submodule 3 (from top to bottom).

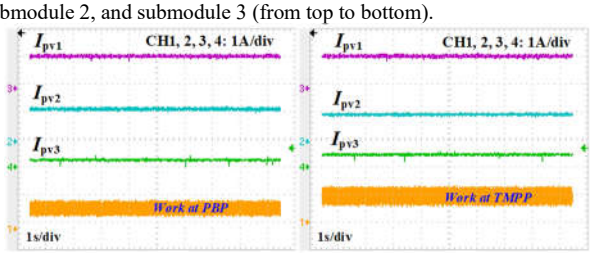

(a) (b)

Fig. 23. The working state of (a) the first partial shading pattern; (b) the second partial shading pattern.

As indicated in [31], the MPPT perturbation step-size must be large enough to guarantee the stability of the centralized least power point tracking (LPPT) control. Thanks for the coupling effect between the submodule-level MPPT algorithm and a centralized LPPT algorithm, the convergence time when the irradiation is decreased by 100W/m^2 was measured as the 40s [31]. In order to improve the convergence speed, the submodule-level control in the proposed algorithm is decoupled from the centralized string current control. Specifically, an open-loop fixed duty-cycle VE control approach is used for submodule-level control, which requires no real-time sensing or communication, as discussed in the aforementioned section. A simple linear formula is used to calculate the reference string current $I_{\text{string,ref}}$ rather than the complicated MPPT tracking process. Thus, both the convergence speed and system stability can be guaranteed. Fig. 24 illustrates the indoor experimental test results under three defined partial shading patterns, and the convergence time of the string current was measured less than 150ms, which presents a 260 times faster convergence speed compared with that in [31] and [32].

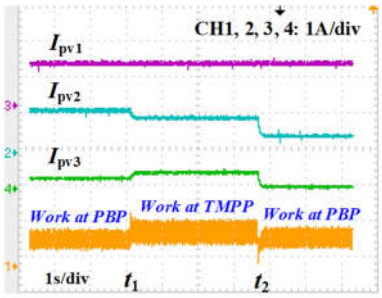

Fig. 24. Indoor experimental test results under three defined partial shading patterns.

C. *Effect of DC-link Capacitance*

In order to evaluate the effect of dc-link capacitance on the proposed algorithm, a dc-link capacitor parallel with load resistor was used to replace a constant voltage source for the experimental evaluation. Two bus capacitances of 2.2mF and 15mF were chosen, and the waveforms of submodule voltage and bus voltage for difference capacitances are shown in Fig. 25 and Fig. 26, respectively.

As illustrated in Fig. 25, for two capacitance values, the variation of the dc-link voltage with respect to the irradiation change is small, which is in accordance with the simulation results. Furthermore, as illustrated in Fig. 26, the transient time for both the PV submodule voltage and dc-link voltage is short, which validates the theoretical analysis of the proposed PBP control.

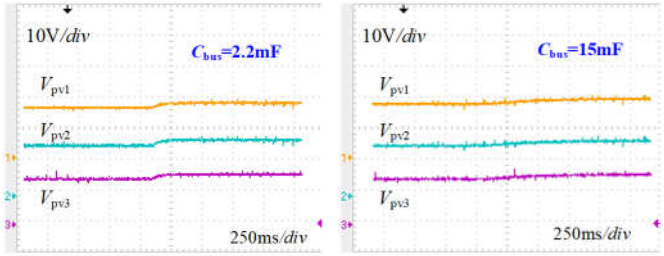

(a) (b)

Fig. 25. Effect of the bus-link capacitance on PV submodule voltage.

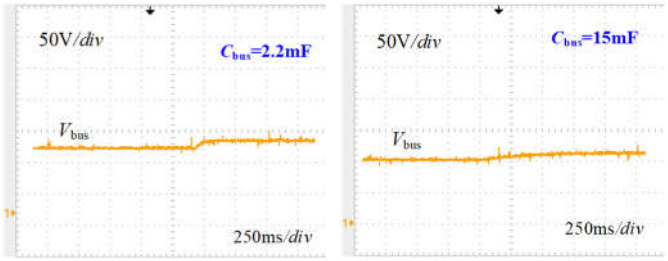

(a) (b)

Fig. 26. Effect of the bus-link capacitance on dc-link voltage.

D. *Outdoor experimental test*

An outdoor filed experiment under a variety of conditions was conducted to evaluate the performance of the proposed algorithm in a practical working condition. Three PV panels (PV-20 SFP2136) connected in series were mounted in a north-facing direction together with the test equipment. Fig. 27 shows the outdoor test bench, which was set similar to the indoor test except that the DC-power supplies with the function of

TABLE VI
TOTAL PROCESSED POWER BY DPP CONVERTERS AND MEASURED EFFICIENCY BY USING DIFFERENT CONTROLS

Shading Case	TMPP			PBP			Hybrid		
	P_{total}	$P_{single,max}$	Efficiency	P_{total}	$P_{single,max}$	Efficiency	P_{total}	$P_{single,max}$	Efficiency
Scenario #1	14.5W	14.5W	92.6%	21.69W	7.23W	92.1%	21.69W	7.23W	92.1%
Scenario #2	11.9W	8.5W	92.8%	14.45W	5.95W	92.4%	11.9W	8.5W	92.8%
Scenario #3	12W	12W	91.4%	12.4W	6.2W	91.4%	12.4W	6.2W	91.4%

TABLE VII
COMPARSION OF CONTROLS FOR PV-BUS ARCHITECTURE

Features	Least power point tracking [31]	Unit-least power point tracking [32]	This work
Submodule-level tracking	MPPT	MPPT	VE
Coupling degree	High	High	Low
Even power distribution	No	Yes	Yes
Requiring local voltage sensing *(submodule-level & module level)*	Yes / No	Yes / No	No / No
Steady-state perturbation oscillation *(submodule-level & module-level)*	Yes / Yes	Yes / Yes	No / No
Algorithm tracking speed *(submodule-level & module-level)*	Slow / medium	Slow / medium	High / high
Interfacing between two-level algorithms	Yes	Yes	No

emulating the photo-diode current have been removed. For the outdoor test, PV submodule 2 is operating without any obstruction interference while PV submodule 3 is shaded by a moving block, and PV submodule 1 is shaded by a fixed leaf. The main experimental results are shown in Fig. 28. Depending on the position of the moving shading block, two shading scenarios can be evaluated. In the first shading scenario, PV submodule 2 is working without any shading, while the other two submodules experience different level partial shading. Under this condition, the optimal string current with the TMPP should be 0.6A, which will show the maximum power stress on a single DPP converter is approximately 8.5W that is less than 10W. Thus, TMPP is implemented rather than the PBP, and the selected string current is 0.6A, as illustrated in Fig. 28. Then, the moving shading block will be regulated toward north a little bit at time instant t_1 so that the shading level of submodule 3 is reduced. Then, submodule 1 and 2 remain in their original working states under the second scenario, which corresponds to the results shown after the time instant t_1. Under the second scenario, with the VE control, the current I_{pv2} is increased from 0.6A to 1A, as shown in Fig. 28. Under this condition, the powers processed by each single DPP converter are P_{dpp1} = 12W, P_{dpp2} = 0W, and P_{dpp3} = 0W, which shows that maximum single power stress is higher than the defined boundary stress. Thus, the control algorithm will change from the TMPP to the PBP to achieve the even power distribution. Thus, the outdoor experimental results under three different conditions validate the effectiveness of the proposed algorithm, which can balance the requirements of efficiency and power stress.

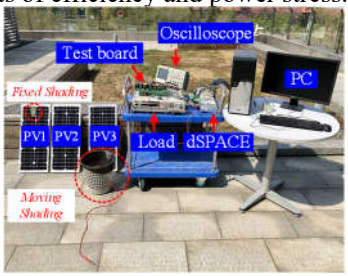

Fig. 27. Outdoor experimental setup.

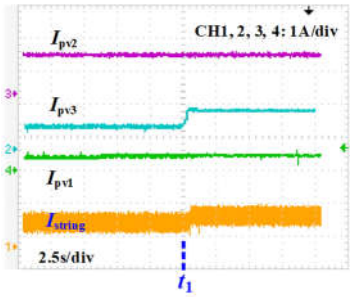

Fig. 28. Outdoor experimental results.

VI. CONCLUSION

This paper provides a novel optimization algorithm for PV-to-bus DPP architecture. Specifically, distributed PV submodule level control and simultaneously, the centralized least power point tracking are implemented to maximize the PV power yield. Compared with complicated true MPPT algorithms, a simple VE control is adopted independently for each PB submodule to reduce the cost for communication among DPP converters. Detailed analysis of the effects of the simple VE on the MPPT efficiency under various working conditions has been provided to support the simple VE control for the practical design. Furthermore, to address the system efficiency and power stress simultaneously, a PBP based optimization algorithm has been proposed to reduce the system cost, size, and implementation complexity, improve the system efficiency, and realize the standardized modular design for DPP converters. Three modes, including the TMPP, PBP, and bypass have been presented with the transition boundaries clearly defined. Both simulation and experimental results under different working conditions are provided to show the performance of the proposed algorithm in terms of steady-state and dynamic performance. The results show that the proposed algorithm can reduce the power rating of DPP converters to half of that with conventional control for worst-case MPP voltage variations, which is beneficial to the improvement of reliability and lifetime. Each PV module is regulated independently without the need for communication. The algorithm implementation complexity

has been significantly simplified. The steady-state perturbation oscillation is largely reduced, and the tracking speed due to the changes in working conditions becomes faster. These advantages of the proposed algorithm will significantly promote the wide application of DPP based PV architecture and better address the photovoltaic partial shading problems. Table VII summarizes the key features of several control strategies for PV-to-bus DPP architecture.

In further, reducing the number of current sensors in submodule-level DPP converters is an important optimization aspect. Similar to the work in [28], by setting the DP converters in discontinuous conducting mode (DCM), the current sensor-less design can be achieved since the submodule current $I_{pv,n}$ can be directly calculated from a formula consisting of submodule voltage and duty cycle. Actually, the bidirectional flyback converter can be tuned at the DCM to achieve the current sensor-less MPPT control. Due to the constraint of the paper page, the design aspect will be presented in the future.

APPENDIX

The MOSFETs used in the experiments are taken and the power loss parameters are set as: $a = 0.11$ and $b = 0.0936$. The real PV panel MSX60W used in the experiments is selected for the calculation. Its MPP current is 3.5A at standard test condition (STC), and the equalized voltage is set as 17V. The worst scenario in (10) is considered and the sum of the submodule currents in the set of K is approximately equal to 0. I_{string} is sweeping while the value of $I_{pv,(n+1)/2}$ is regulated to infinitely approach 3.5A. Under the defined conditions, the relationship can be derived as: $0.87k \leqslant 17$. the conclusion is that when k is less than 19, which corresponds to the number of PV submodules n less than 39, the slope of the curve is always negative when $k - p < 0$. Considering the submodule-based DPP architecture and the practical parameters for PV modules and power devices, the condition in (10) can be naturally fulfilled.

REFERENCE

[1] G. Velasco-Quesada, F. Guinjoan-Gispert, R. Pique-Lopez, M. Roman-Lumbreras, and A. Conesa-Roca, "Electrical PV Array Reconfiguration Strategy for Energy Extraction Improvement in Grid-Connected PV Systems," *IEEE Transactions on Industrial Electronics,* vol. 56, no. 11, pp. 4319-4331, 2009.

[2] A. Mäki and S. Valkealahti, "Power Losses in Long String and Parallel-Connected Short Strings of Series-Connected Silicon-Based Photovoltaic Modules Due to Partial Shading Conditions," *IEEE Transactions on Energy Conversion,* vol. 27, no. 1, pp. 173-183, 2012.

[3] H. Zheng, S. Li, and J. Proano, "PV energy extraction characteristic study under shading conditions for different converter configurations," in *2012 IEEE Power and Energy Society General Meeting*, 2012, pp. 1-8.

[4] F. A. Silva, "Power Electronics and Control Techniques for Maximum Energy Harvesting in Photovoltaic Systems (Femia, N. et al; 2013) [Book News]," *IEEE Industrial Electronics Magazine,* vol. 7, no. 3, pp. 66-67, 2013.

[5] S. M. MacAlpine, R. W. Erickson, and M. J. Brandemuehl, "Characterization of Power Optimizer Potential to Increase Energy Capture in Photovoltaic Systems Operating Under Nonuniform Conditions," *IEEE Transactions on Power Electronics,* vol. 28, no. 6, pp. 2936-2945, 2013.

[6] M. C. Alonso-García, J. M. Ruiz, and F. Chenlo, "Experimental study of mismatch and shading effects in the I–V characteristic of a photovoltaic module," *Solar Energy Materials and Solar Cells,* vol. 90, no. 3, pp. 329-340, 2006/02/15/ 2006.

[7] C. Deline, "Partially shaded operation of a grid-tied PV system," in *2009 34th IEEE Photovoltaic Specialists Conference (PVSC)*, 2009, pp. 001268-001273.

[8] L. Gao, R. A. Dougal, S. Liu, and A. P. Iotova, "Parallel-Connected Solar PV System to Address Partial and Rapidly Fluctuating Shadow Conditions," *IEEE Transactions on Industrial Electronics,* vol. 56, no. 5, pp. 1548-1556, 2009.

[9] G. R. Walker and P. C. Sernia, "Cascaded DC-DC converter connection of photovoltaic modules," *IEEE Transactions on Power Electronics,* vol. 19, no. 4, pp. 1130-1139, 2004.

[10] L. Linares, R. W. Erickson, S. MacAlpine, and M. Brandemuehl, "Improved Energy Capture in Series String Photovoltaics via Smart Distributed Power Electronics," in *2009 Twenty-Fourth Annual IEEE Applied Power Electronics Conference and Exposition*, 2009, pp. 904-910.

[11] A. I. Bratcu, I. Munteanu, S. Bacha, D. Picault, and B. Raison, "Cascaded DC–DC Converter Photovoltaic Systems: Power Optimization Issues," *IEEE Transactions on Industrial Electronics,* vol. 58, no. 2, pp. 403-411, 2011.

[12] R. C. N. Pilawa-Podgurski and D. J. Perreault, "Submodule Integrated Distributed Maximum Power Point Tracking for Solar Photovoltaic Applications," *IEEE Transactions on Power Electronics,* vol. 28, no. 6, pp. 2957-2967, 2013.

[13] C. Deline and S. MacAlpine, "Use conditions and efficiency measurements of DC power optimizers for photovoltaic systems," in *2013 IEEE Energy Conversion Congress and Exposition*, 2013, pp. 4801-4807.

[14] O. Khan, W. Xiao, and H. H. Zeineldin, "Gallium-Nitride-Based Submodule Integrated Converters for High-Efficiency Distributed Maximum Power Point Tracking PV Applications," *IEEE Transactions on Industrial Electronics,* vol. 63, no. 2, pp. 966-975, 2016.

[15] O. Khan and W. Xiao, "An Efficient Modeling Technique to Simulate and Control Submodule-Integrated PV System for Single-Phase Grid Connection," *IEEE Transactions on Sustainable Energy,* vol. 7, no. 1, pp. 96-107, 2016.

[16] F. Wang, T. Zhu, F. Zhuo, H. Yi, S. Shi, and X. Zhang, "Analysis and Optimization of Flexible MCPT Strategy in Submodule PV Application," *IEEE Transactions on Sustainable Energy,* vol. 8, no. 1, pp. 249-257, 2017.

[17] O. Khan, W. Xiao, and M. S. E. Moursi, "A New PV System Configuration Based on Submodule Integrated Converters," IEEE Transactions on Power Electronics, vol. 32, no. 5, pp. 3278-3284, 2017.

[18] S. Qin, C. B. Barth, and R. C. N. Pilawa-Podgurski, "Enhancing Microinverter Energy Capture With Submodule Differential Power Processing," *IEEE Transactions on Power Electronics,* vol. 31, no. 5, pp. 3575-3585, 2016.

[19] O. Khan and W. Xiao, "Review and qualitative analysis of submodule-level distributed power electronic solutions in PV power systems," Renewable and Sustainable Energy Reviews, vol. 76, pp. 516-528, 2017/09/01/ 2017.

[20] G. R. Walker and J. C. Pierce, "Photovoltaic DC-DC module integrated converter for novel cascaded and bypass grid connection topologies — Design and optimization," in *2006 37th IEEE Power Electronics Specialists Conference*, 2006, pp. 1-7.

[21] Y. Nimni and D. Shmilovitz, "A returned energy architecture for improved photovoltaic systems efficiency," in *Proceedings of 2010 IEEE International Symposium on Circuits and Systems*, 2010, pp. 2191-2194.

[22] P. S. Shenoy and P. T. Krein, "Differential Power Processing for DC Systems," *IEEE Transactions on Power Electronics,* vol. 28, no. 4, pp. 1795-1806, 2013.

[23] P. S. Shenoy, K. A. Kim, B. B. Johnson, and P. T. Krein, "Differential Power Processing for Increased Energy Production and Reliability of Photovoltaic Systems," *IEEE Transactions on Power Electronics,* vol. 28, no. 6, pp. 2968-2979, 2013.

[24] J. T. Stauth, M. D. Seeman, and K. Kesarwani, "A Resonant Switched-Capacitor IC and Embedded System for Sub-Module Photovoltaic Power Management," *IEEE Journal of Solid-State Circuits,* vol. 47, no. 12, pp. 3043-3054, 2012.

[25] R. Sangwan, K. Kesarwani, and J. T. Stauth, "High-density power converters for sub-module photovoltaic power management," in *2014 IEEE Energy Conversion Congress and Exposition (ECCE)*, 2014, pp. 3279-3286.

[26] S. Qin, S. T. Cady, A. D. Domínguez-García, and R. C. N. Pilawa-Podgurski, "A Distributed Approach to Maximum Power Point Tracking for Photovoltaic Submodule Differential Power Processing," *IEEE Transactions on Power Electronics,* vol. 30, no. 4, pp. 2024-2040, 2015.
[27] S. Qin and R. C. N. Pilawa-Podgurski, "Sub-module differential power processing for photovoltaic applications," in *2013 Twenty-Eighth Annual IEEE Applied Power Electronics Conference and Exposition (APEC)*, 2013, pp. 101-108.
[28] C. Olalla, D. Clement, M. Rodriguez, and D. Maksimovic, "Architectures and Control of Submodule Integrated DC-DC Converters for Photovoltaic Applications," *IEEE Transactions on Power Electronics,* vol. 28, no. 6, pp. 2980-2997, 2013.
[29] J. Du, R. Xu, X. Chen, Y. Li, and J. Wu, "A novel solar panel optimizer with self-compensation for partial shadow condition," in *2013 Twenty-Eighth Annual IEEE Applied Power Electronics Conference and Exposition (APEC)*, 2013, pp. 92-96.
[30] J. H. Park and K. T. Kim, "Multi-output differential power processing system using boost-flyback converter for voltage balancing," in *2017 International Conference on Recent Advances in Signal Processing, Telecommunications & Computing (SigTelCom)*, 2017, pp. 139-142.
[31] Y. T. Jeon, H. Lee, K. A. Kim, and J. H. Park, "Least Power Point Tracking Method for Photovoltaic Differential Power Processing Systems," *IEEE Transactions on Power Electronics,* vol. 32, no. 3, pp. 1941-1951, 2017.
[32] Y. T. Jeon and J. h. Park, "Unit-Minimum Least Power Point Tracking for the Optimization of Photovoltaic Differentional Power Processing Systems," *IEEE Transactions on Power Electronics,* pp. 1-1, 2018.
[33] K. Sun, Z. Qiu, H. Wu, and Y. Xing, "Evaluation on High-Efficiency Thermoelectric Generation Systems Based on Differential Power Processing," *IEEE Transactions on Industrial Electronics,* vol. 65, no. 1, pp. 699-708, 2018.
[34] Y. Levron, D. R. Clement, B. Choi, C. Olalla, and D. Maksimovic, "Control of Submodule Integrated Converters in the Isolated-Port Differential Power-Processing Photovoltaic Architecture," *IEEE Journal of Emerging and Selected Topics in Power Electronics,* vol. 2, no. 4, pp. 821-832, 2014.
[35] B. Choi, D. Clement, and D. Maksimovic, "A CMOS controller for submodule integrated converters in photovoltaic systems," in *2014 IEEE 15th Workshop on Control and Modeling for Power Electronics (COMPEL)*, 2014, pp. 1-6.
[36] C. Olalla, C. Deline, D. Clement, Y. Levron, M. Rodriguez, and D. Maksimovic, "Performance of Power-Limited Differential Power Processing Architectures in Mismatched PV Systems, " *IEEE Transactions on Power Electronics,* vol. 30, no. 2, pp. 618-631, 2015.
[37] R. Bell and R. C. N. Pilawa-Podgurski, "Decoupled and Distributed Maximum Power Point Tracking of Series-Connected Photovoltaic Submodules Using Differential Power Processing," *IEEE Journal of Emerging and Selected Topics in Power Electronics,* vol. 3, no. 4, pp. 881-891, 2015.
[38] E. Candan, P. S. Shenoy, and R. C. N. Pilawa-Podgurski, "A Series-Stacked Power Delivery Architecture With Isolated Differential Power Conversion for Data Centers," *IEEE Transactions on Power Electronics,* vol. 31, no. 5, pp. 3690-3703, 2016.
[39] G. Chu, H. Wen, L. Jiang, Y. Hu, and X. Li, "Bidirectional flyback based isolated-port submodule differential power processing optimizer for photovoltaic applications," *Solar Energy,* vol. 158, pp. 929-940, 2017/12/01/ 2017.
[40] K. A. Kim, P. S. Shenoy, and P. T. Krein, "Converter Rating Analysis for Photovoltaic Differential Power Processing Systems," *IEEE Transactions on Power Electronics,* vol. 30, no. 4, pp. 1987-1997, 2015.
[41] P. S. Shenoy, B. Johnson, and P. T. Krein, "Differential power processing architecture for increased energy production and reliability of photovoltaic systems," in *2012 Twenty-Seventh Annual IEEE Applied Power Electronics Conference and Exposition (APEC)*, 2012, pp. 1987-1994.
[42] G. Chu and H. Wen, "Design and Optimization of PV-Isolated-Port Photovoltaic Differential Power Porcessing System," in *2018 IEEE International Conference on Power Electronics, Drives and Energy Systems (PEDES)*, 2018, pp. 1-6.
[43] E. Candan, A. Stillwell and R. C. N. Pilawa-Podgurski, "A reliability assessment of series-stacked servers with server-to-bus differential power processing," *2016 IEEE International Telecommunications Energy Conference (INTELEC)*, Austin, TX, 2016, pp. 1-7.
[44] R. Bell, "Power management of series connected photovoltaic submodules using the element-to-virtual bus differential power processing architecture," M.S. thesis, Dept. Elect. Comput. Eng., Univ. Illinois at Urbana–Champaign, Champaign, IL, USA, 2014.
[45] International Rectifier , "Understanding and Using Power MOSFET Reliabaility Data", POWER MOSFET APPLICATION NOTES, 1987.
[46] G. Graditi, D. Colonnese and N. Femia, "Efficiency and reliability comparison of DC-DC converters for single phase grid connected photovoltaic inverters, " *SPEEDAM 2010*, Pisa, 2010, pp. 140-147.
[47] P. S. Shenoy, "Improving performance, efficiency, and reliability of DC-DC conversion system by using differential power processing," Ph.D. Dissertation, Dept. Elect. Comput. Eng., Univ. Illinois at Urbana–Champaign, Champaign, IL, USA, 2012.

Guanying Chu (S'19) received the B.S. and M.S. degree in Electrical and Electronic Engineering from the University of Sheffield, Sheffield, UK, in 2014 and 2015 respectively. He is currently working toward the Ph.D. degree at the University of Liverpool, UK. His current research interests include bidirectional dc-dc converter, digital control, and photovoltaic applications.

Huiqing Wen (M'13-SM'17) received his B.S. and M.S. degrees in Electrical Engineering from Zhejiang University, Hangzhou, China, in 2002 and 2006, respectively; and his Ph.D. degree in Electrical Engineering from the Chinese Academy of Sciences, Beijing, China, in 2009. From 2009 to 2010, he was an Electrical Engineer working in the Research and Development Center, GE (China) Co., Ltd., Shanghai, China. From 2010 to 2011, he was an Engineer at the China Coal Research Institute, Beijing, China. From 2011 to 2012, he was a Postdoctoral Fellow at the Masdar Institute of Science and Technology, Abu Dhabi, United Arab Emirates.

He is presently working as an Associate Professor at the Xi'an Jiaotong-Liverpool University, Suzhou, China. His current research interests include bidirectional DC-DC converters, power electronics in flexible AC transmission applications, electrical vehicles, and high-power, three-level electrical driving systems.

Yihua Hu (M'13-SM'15) received the B.S. degree in electrical engineering in 2003, and the Ph.D. degree in power electronics and drives in 2011, both at China University of Mining and Technology. Between 2011 and 2013, he was with the College of Electrical Engineering, Zhejiang University as a Postdoctoral Fellow. Between 2013 and 2015, he worked as a Research Associate at the power electronics and motor drive group, the University of Strathclyde. Between 2016 and 2019, he was a Lecturer at the Department of Electrical Engineering and Electronics, University of Liverpool (UoL). Currently, he is a Reader at Electronics Engineering Department at The University of York (UoY). He has published 100 papers in IEEE Transactions journals. His research interests include renewable generation, power electronics converters & control, electric vehicle, more electric ship/aircraft, smart energy system and non-destructive test technology. He is the associate editor of IEEE Transactions on Industrial Electronics, IET Renewable Power Generation, IET Intelligent Transport Systems and Power Electronics and Drives.

Lin Jiang (M'00) received his B.S. and M.S. degrees in Electrical Engineering from the Huazhong University of Science and Technology, Wuhan, China, in 1992 and 1996, respectively; and his Ph.D. degree in Electrical Engineering from the University of Liverpool, Liverpool, ENG, UK, in 2001. He is presently working as a Reader of Electrical Engineering at the University of Liverpool. His current research interests include the optimization and control of smart grids, electrical machines, power electronics and renewable energy.

Yong Yang (M'15) received the B.S. degree in automation from Xiangtan University, Xiangtan, China, in 2003, the M.S. degree in Electrical Engineering from Guizhou University, Guiyang, China, in 2006, and the Ph.D. degree in Electrical Engineering from Shanghai University, Shanghai, China, in 2010.

He is currently an associate professor with the School of Rail Transportation, Soochow University. From December 2017 to December 2018, he was a Visiting Scholar with Center for High Performance Power Electronics (CHPPE) of the Ohio State University, Columbus, USA. He has authored more than 60 journal and conference papers. His current research interests include model predictive control in power electronic converters, distributed energy resource interfacing and high-performance motor drive control.

Yiwang Wang received the B.S. degree in electrical engineering and automation from Kunming University of Science and Technology, Kunming, China, in 2005, the M.S. degree in Power Electronics from Jiangnan University, Wuxi, China, in 2008. He is currently pursuing the Ph.D. degree in electrical engineering at School of Electronic, Information and Electrical Engineering in Shanghai Jiao Tong University.

He is currently an Associate Professor with Suzhou Vocational University, Suzhou, China. From June 2016 until June 2017, he was a visiting scholar in the CURENT research center, University of Tennessee, Knoxville, TN, USA. His research interests include power electronics intelligent control, the application of power electronics and renewable energy generation.